Journal of Electroanalytical Chemistry 904 (2022) 115928

Contents lists available at ScienceDirect

Journal of Electroanalytical Chemistry

journal homepage: www.elsevier.com/locate/jelechem

Designing coral-like Fe_2O_3-regulated Se-rich $CoSe_2$ heterostructure as a highly active and stable oxygen evolution electrocatalyst for overall water splitting

Zixia Wan [a,b], Qiuting He [a], Yuan Qu [a], Jiaxin Dong [a,*], Elvis Shoko [d], Puxuan Yan [a], Tayirjan Taylor Isimjan [c,*], Xiulin Yang [a,*]

[a] Guangxi Key Laboratory of Low Carbon Energy Materials, School of Chemistry and Pharmaceutical Sciences, Guangxi Normal University, Guilin 541004, China
[b] Zhuhai People's Hospital (Zhuhai Hospital Affiliated with Jinan University), Zhuhai 519070, China
[c] Saudi Arabia Basic Industries Corporation (SABIC) at King Abdullah University of Science and Technology (KAUST), Thuwal 23955-6900, Saudi Arabia
[d] Department of Chemistry, University of Liverpool, Liverpool L69 3BX, United Kingdom

ARTICLE INFO

Keywords:
Fe_2O_3-$CoSe_2$@Se
Coral-like structure
Synergistic effect
Oxygen evolution
Water splitting

ABSTRACT

The electrocatalytic oxygen evolution reaction (OER) is the bottleneck to overall water splitting because of the slow kinetics of the four-electron transfer process. Therefore, it is of great significance to develop OER electrocatalysts with high activity, long durability, and scalability. Herein, we present a selenium-coated cobalt selenide ($CoSe_2$@Se) catalyst that was first synthesized by *in-situ* growth on carbon cloth (CC) surface by hydrothermal method, followed by soaking treatment to prepare a three-dimensional coral-like Fe_2O_3-$CoSe_2$@Se/CC composite. Electrochemical studies revealed that the optimized Fe_2O_3-$CoSe_2$@Se/CC catalyst only requires 250 mV to reach 10 mA cm^{-2} current density, yields a small Tafel slope (50.2 mV dec^{-1}), and has good stability (10 mA cm^{-2}@70 h) in the electrocatalytic OER process. The overall water splitting using Fe_2O_3-$CoSe_2$@Se/CC as anode only requires 1.58 and 1.69 V to achieve 10 and 100 mA cm^{-2}, respectively, much better than most previously reported catalysts. Analysis showed that the three-dimensional coral-like morphology exposing more active sites and the synergy between different species (giving rise to, *inter alia*, a favorable electronic structure that lowers the electrode overpotential) are the key to the observed improved electrocatalytic performance. This work provides a novel strategy for the rational design of nanostructured OER hybrid catalysts in the future.

1. Introduction

With the increased depletion rate of fossil fuels, exploring renewable energy sources has become exceptionally important [1,2]. Nevertheless, the primary sources of renewable energy, such as wind and solar power, are intermittent because of changes on the seasonal, daily, and regional scales [3,4]. As an alternative, electrochemical water splitting is a very much preferred approach for establishing a sustainable and environmentally clean energy source since it produces carbon-free, renewable, and clean hydrogen for energy generation [5,6]. The critical challenge for water-splitting under alkaline conditions is improving the kinetically slow, rate-limiting four-electron transfer OER process ($4OH^- \rightarrow 2H_2O + O_2 + 4e^-$) [7–10], where the OER determines the overall efficiency of a water-splitting system. Currently, IrO_2 and RuO_2 are widely regarded as the benchmark robust OER electrocatalysts. However, high cost and scarcity seriously hinder their widespread application [11,12]. Therefore, the development of highly active and low-cost OER electrocatalysts to replace precious metals is greatly desirable.

Motivated by this situation, a lot of attention has been given to develop the transition metal based OER catalysts, due to their high earth abundance, special e_g orbitals, and unique electronic structure [13,14]. In particular, bimetallic composites possess better OER performance compared to monometallic materials because the synergistic effect of electronic tuning will affect the reaction kinetics [11,15]. Thus far, significant efforts have been devoted to developing non-precious metal catalysts of transition metal oxides [16], (oxy)hydroxides [17,18], phosphates [19], sulfides [20], and so on. Interestingly, selenides have high metallic properties, large relative ionic radius, and small ionization energy, all beneficial to OER performance [21]. For

* Corresponding authors.
E-mail addresses: chemdjx@gxnu.edu.cn (J. Dong), isimjant@sabic.com (T. Taylor Isimjan), xlyang@gxnu.edu.cn (X. Yang).

https://doi.org/10.1016/j.jelechem.2021.115928
Received 26 July 2021; Received in revised form 6 November 2021; Accepted 28 November 2021
Available online 1 December 2021

example, A. T. Sweis and colleagues successfully synthesized a nickel selenide-based compound, and the catalyst reached a current density of 10 mA cm^{-2} at a low overpotential of 290 mV, showing outstanding activity [22]. However, there is no report on the selenide-based OER catalyst showing a stable performance at high current densities (200 ~ 400 mA cm^{-2}) that are essential for industrial applications [23]. Building on our previous studies [24–27], we constructed a novel Fe_2O_3-manipulated Se-rich $CoSe_2$ hybrid OER catalyst working at high current density for the first time.

In this work, we report a Fe_2O_3-$CoSe_2$@Se/CC hybrid catalyst synthesized on CC through a controllable *in-situ* hydrothermal method and a subsequent soaking treatment. Various characterizations explored the crystal structure, microscopic morphology, surface chemical state, and actual composition of the hybrid material. The electrocatalytic OER performance in the three-electrode system proves that the catalyst has both good electrocatalytic activity and stability superior to most of the reported OER catalysts. Moreover, the two-electrode electrolyzer system simulating industrial conditions also shows remarkable overall water splitting activity and stability.

2. Experimental section

2.1. Synthesis of $CoSe_2$@Se/CC

All chemicals used are of analytical grade and were used directly without further purification. Firstly, the carbon cloth (CC) was cut into 1 cm × 1 cm square pieces. Then the CC was sonicated for 3 times in 0.5 M hydrochloric acid, deionized water, and ethanol successively, followed by drying under vacuum at 60 °C for use. And then, Co$(NO_3)_2{\cdot}6H_2O$ and Se powders at a molar ratio of 4/1 were dissolved in 35 mL of ethylene glycol and 35 mL of deionized water in a beaker containing a clean stirrer. Subsequently, the resulting solution and CC were transferred into a Teflon-lined stainless autoclave (90 mL) and heated at 180 °C for 12 h. After cooling to room temperature, the $CoSe_2$@Se modified CC was washed with abundant deionized water, and vacuum-dried at 60 °C for 3 h to obtain the catalyst.

2.2. Synthesis of Fe_2O_3-$CoSe_2$@Se/CC-xh

A facile method through direct mixing and stirring $FeSO_4{\cdot}7H_2O$ with $CoSe_2$@Se/CC was devised, in which 0.1 M $FeSO_4$ was initially prepared by weighing 1.39 g $FeSO_4{\cdot}7H_2O$ and dissolving in 50 mL H_2O, and then a piece of $CoSe_2$@Se/CC was immersing into the solution under constant stirring for different times. The obtained composites are denoted as Fe_2O_3-$CoSe_2$@Se/CC-xh (x = 0.5, 1.0, 1.5) according to the total soaking time. The loading of the catalyst is approximately 1.1 ~ 2.2 mg cm^{-2} weighed by a microbalance (**Table S1**). The Fe, Co and Se contents were determined by ICP-AES (**Table S2**), and the Se content remained the same with the different immersion times.

2.3. Synthesis of RuO_2/CC and Pt/C/CC

As a comparison, the RuO_2 or Pt/C catalyst is directly supported on the carbon cloth by titration. The ultimate capacity of contrast catalysts is about 1.0 mg cm^{-2}. The prepared catalysts are dried at room temperature and then used directly.

2.4. Electrochemical measurements

Electrochemical measurements were carried out in a standard three-electrode system operated by a VMP3B-2x2 electrochemical analyzer (CH Instruments, Inc, France). Catalysts loaded on CC were used as the working electrode (1 × 1 cm^2), a saturated calomel electrode (SCE) as the reference, and a carbon plate as the counter electrode. Electrochemical measurements of those catalysts were implemented in 1.0 M KOH solution. Polarization curves were acquired using linear sweep voltammetry (LSV) at a scan rate of 5 mV s^{-1}. Electrochemical impedance spectroscopy (EIS) measurements were carried out in the frequency range of 200 kHz ~ 0.1 Hz. The chronopotentiometry was utilized for long-term stability tests. All potentials measured were calibrated to the RHE using the following equation: E(RHE) = E (SCE) + 0.2415 V + 0.059·pH (Fig. S1). All electrochemical data are corrected against ohm potential drop. The CV tests on catalysts are characterized at a varied of scan rates in 1.0 M KOH solution to obtain the electrochemical double-layer capacitance (C_{dl}). The two-electrode overall water splitting test is obtained by using Fe_2O_3-$CoSe_2$@Se/CC as the anode and Pt/C/CC as the cathode with a scan rate of 5 mV s^{-1} in 1.0 M KOH solution.

3. Results and discussion

3.1. Synthetic strategy and crystallinity analysis

The Fe_2O_3-$CoSe_2$@Se/CC material is synthesized by a facile two-step process, including a conventional hydrothermal process to form a $CoSe_2$@Se/CC precursor and subsequent soaking in $FeSO_4{\cdot}7H_2O$ solution for different times (Fig. 1**a**). Unless specified, the Fe_2O_3-$CoSe_2$@Se/CC catalyst discussed below refers to the soaking time of 1.0 h.

The X-ray diffraction (XRD) pattern of the $CoSe_2$@Se/CC material (Fig. 1**b**) shows that it is mainly composed of cubic $CoSe_2$ (JCPDS: 88-1712) [28] and hexagonal Se (JCPDS: 06-0362) [29]. After soaking in the $FeSO_4$ solution (Fig. 1**c**), new strong peaks corresponding to tetragonal Fe_2O_3 (JCPDS: 25-1402) [30] along with the diffraction peaks of Se and $CoSe_2$. The changes in the crystal phase structure indicate that new hybrid materials have been formed after soaking in the Fe species for different times.

3.2. Microstructure and composition analysis

The morphology and microstructure of the hybrid materials were investigated by scanning electron microscopy (SEM) and transmission electron microscopy (TEM). The SEM image of Fig. 2**a** shows that the coral-like $CoSe_2$@Se is loosely anchored on the surface of the CC. The high-magnification SEM image shows that the lateral size of the 3D structure is about 5–6 μm. The morphology of the hybrid material gradually evolves from somewhat fluffy at 0.5 h (**Fig. S2a**), to denser at 1.0 h (Fig. 2**b**), and then to agglomeration and collapse at 1.5 h (**Fig. S2b**). ICP-AES test results indicate that the percentage of Fe in different composites gradually increases with the soaking time (**Table S2**), which is consistent with the observed morphological evolution from SEM analysis and our intuitive expectation.

The TEM study was performed on an ultrasound exfoliated Fe_2O_3-$CoSe_2$@Se sample. The images reveal that the 3D coral-like structure is composed of intersected nanosheets (Fig. 2**c**). High-resolution TEM image shows different types of lattice fringes. For example, lattice spacings of 0.18, 0.25, and 0.30 nm correspond to $CoSe_2$ (311), Fe_2O_3 (119) and Se (101) crystal planes (Fig. 2**d**) [31–33], respectively. As a result, the $CoSe_2$ and Fe_2O_3 components are intertwined, while Se species are mainly distributed in the outer layer. The HAADF-STEM and relative elemental mappings of Fe_2O_3-$CoSe_2$@Se prove the uniform distribution of Co, Fe and O in the hybrid structure, with Se predominantly in the outer layer (Fig. 2**e**).

Thermogravimetric analysis (TGA) was used to monitor the mass loss during the pyrolysis of Fe_2O_3-$CoSe_2$@Se-1.0 h and $CoSe_2$@Se under N_2 atmosphere (25 °C to 900 °C and heating rate of 5 °C min^{-1}). As shown in **Fig. S3a, a** weight loss at 64 °C is associated with adsorbed water [34]. The sharp exothermic peak between 300 and 510 °C indicates a severe weight loss due to Se sublimation and

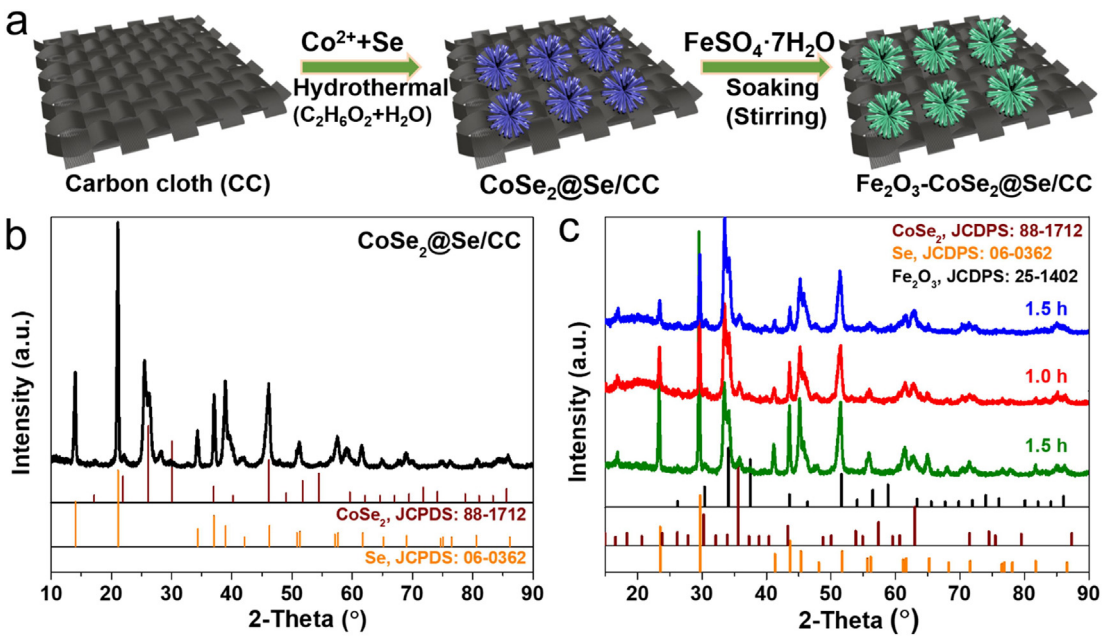

Fig. 1. (a) Schematic diagram of the synthesis process of Fe_2O_3-$CoSe_2$@Se/CC. X-ray diffraction (XRD) patterns of (b) $CoSe_2$@Se/CC and (c) Fe_2O_3-$CoSe_2$@Se/CC for different immersion times of Fe species.

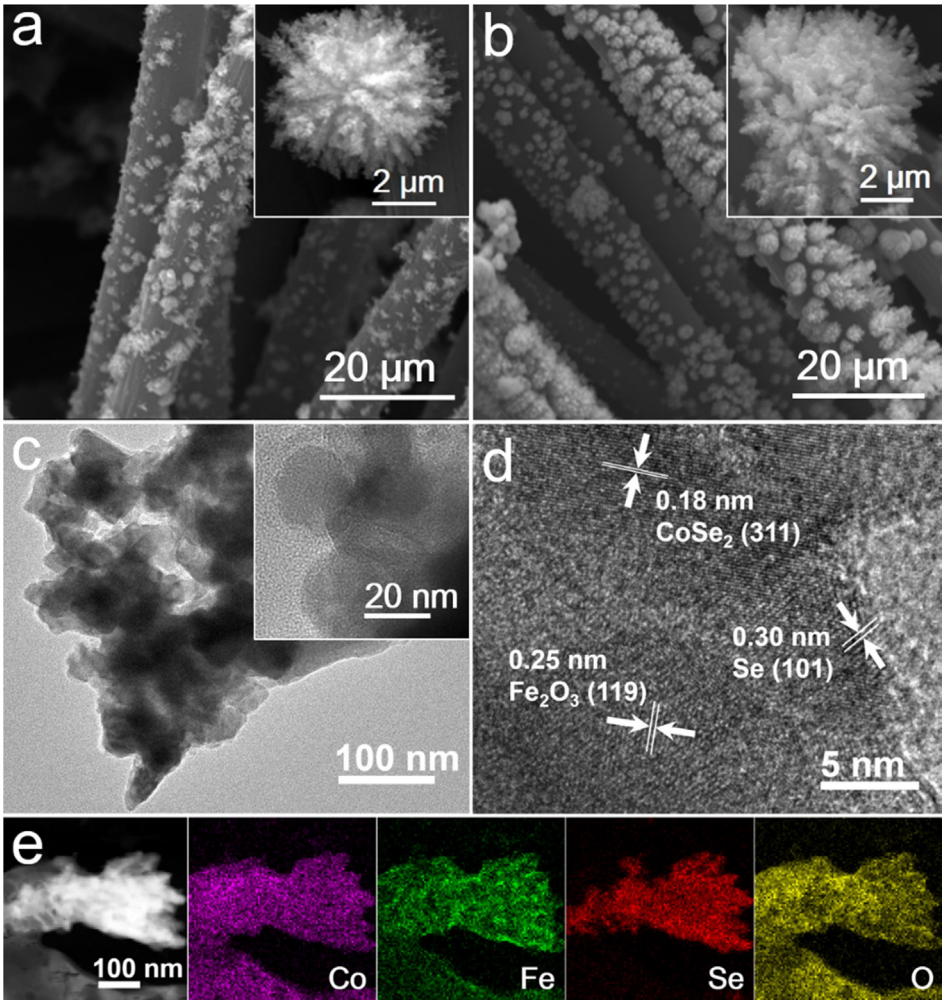

Fig. 2. SEM images of (a) $CoSe_2$@Se/CC and (b) Fe_2O_3-$CoSe_2$@Se/CC (Inset: High magnification SEM images). (c) TEM with inset enlarged scale and (d) high-resolution TEM images of Fe_2O_3-$CoSe_2$@Se. (e) HAADF-STEM image of Fe_2O_3-$CoSe_2$@Se/CC and corresponding elemental mappings of Co, Fe, Se and O.

thermal decomposition of $CoSe_2$ (**Figure S3b)** [31,35,36]. The difference in location is due to the strong interaction between the introduced Fe_2O_3 and $CoSe_2$@Se. In addition, the mass loss of $CoSe_2$@Se was significantly different from Fe_2O_3-$CoSe_2$@Se-1.0 h under the same conditions due to the different composition.

3.3. Chemical state analysis

X-ray photoelectron spectroscopy (XPS) characterization was performed to further study the elemental composition and chemical states of different materials. The survey spectrum of Fe_2O_3-$CoSe_2$@Se/CC show that Fe, Co, Se, C and O are present in the composite (**Fig. S4a)**. Among them, the high-resolution XPS spectrum of C 1 *s* is revised to C═C (284.0 eV), and C—C (284.8 eV) and C—O (286.0 eV) as calibration standards (**Fig. S4b)** [25,37,38]. The high-resolution Co 2*p* XPS spectrum reveals the three pairs of peaks in Fig. 3**a**. For Co $2p_{3/2}$, the binding energies at 778.1, 780.5 and 784.9 eV correspond to the Co-Se bond, Co-O bond and a satellite peak [39,40], respectively. Compared to $CoSe_2$@Se/CC, the binding energy of the Co-O bond of the Fe_2O_3-$CoSe_2$@Se/CC catalyst has a positive shift of 0.49 eV, indicating that there was strong electron interaction between the introduced Fe_2O_3 and partially oxidized $CoSe_2$@Se species, resulting in electron enrichment of the Fe_2O_3 species [26,41]. The high-resolution Se 3*d* region can be deconvoluted into Se $3d_{5/2}$ and $3d_{3/2}$ peaks, of which the two prominent Se $3d_{5/2}$ peaks at 54.2 and 55.1 eV are assigned to Se_2^{2-} and Se [42], while the 58.9 eV binding energy is typical SeO_x species (Fig. 3**b)** [43]. In Fig. 3**c**, the high-resolution Fe $2p_{3/2}$ XPS spectra of Fe_2O_3-$CoSe_2$@Se/CC catalyst can be deconvoluted at approximately 710.6, 712.9 and 717.0 eV binding energies attributable to Fe^{2+}, Fe^{3+} and satellite peak signals [44,45], indicating that the Fe^{3+} species is the dominant component of the material. In addition, the high-resolution O 1 *s* species of the Fe_2O_3-$CoSe_2$@Se/CC catalyst was also explored (Fig. 3**d)**, in which the four signal peaks generated at 530.2, 530.8, 531.7 and 532.8 eV were attributed to Fe/Co-O, oxygen vacancies, adsorbed C═O bond, and adsorbed H_2O/C—O bond [46], respectively. The analysis found that the area content ratio of oxygen vacancies in Fe_2O_3-$CoSe_2$@Se/CC is as high as 44.2%, which is much higher than that in $CoSe_2$@Se/CC (34.9%, **Fig. S4c)** indicating around 10% oxygen vacancies contributed by Fe_2O_3. A large number of studies have found that a high percentage of oxygen vacancies can help regulate the adsorption and desorption of reactants on the surface of the catalyst during the OER process, thereby greatly improving the catalytic activity of OER [47,48].

3.4. Electrochemical OER and overall water splitting analysis

The OER performances of catalysts were further assessed by linear sweep voltammetry (LSV) at a scan rate of 5 mV s^{-1} in 1.0 M KOH solution, and all LSV polarization curves are processed by *iR* compensation as well as RHE correction (**Fig. S1)**. As shown in Fig. 4**a**, the Fe_2O_3-$CoSe_2$@Se/CC-1.0 h electrocatalyst exerts a low overpotential of 252 mV at 10 mA cm^{-2}, which is obviously lower than that of Fe_2O_3-$CoSe_2$@Se-0.5 h (307 mV), Fe_2O_3-$CoSe_2$@Se-1.5 h (290 mV), $CoSe_2$@Se (359 mV) and state of the art RuO_2 (275 mV). In particular, the catalyst still has the best OER catalytic performance among all the catalysts even at high current density (>100 mA cm^{-2}). The analysis found that the introduction of Fe_2O_3 species greatly improved the OER catalytic performance of $CoSe_2$@Se/CC, indicating the synergy between the two components. The regulation of different content of Fe_2O_3 species on catalytic performance is attributed to the number of active sites exposed by the two cooperative heterojunctions [49]. Therefore, only an appropriate amount of Fe_2O_3 species can maximize OER catalytic performance (**Table S2)**. Moreover, the Fe_2O_3-$CoSe_2$@Se/CC catalyst also showed the lowest Tafel slope (50.2 mV dec^{-1}) among all the catalysts, evidencing the fast reaction kinetics (Fig. 4**b)** [50].

In order to clarify the possible reasons for the outstanding OER performance of Fe_2O_3-$CoSe_2$@Se/CC-1.0 h, we further evaluated the electrochemical double layer capacitance (C_{dl}) to reveal the electrochemical surface area (ECSA) (**Fig. S5)** [51,52]. In Fig. 4**c**, the Fe_2O_3-$CoSe_2$@Se/CC-1.0 h catalyst possesses the highest C_{dl} of 48.6 mF cm^{-2} compared with the Fe_2O_3-$CoSe_2$@Se-0.5 h (15.8 mF cm^{-2}), Fe_2O_3-$CoSe_2$@Se-1.5 h (10.4 mF cm^{-2}), and $CoSe_2$@Se (29.1 mF cm^{-2}) catalysts by evaluating CV curves in non-Faradaic potential regions [25]. The ECSA is calculated by the equation of $A_{ECSA} = C_{dl}/C_s$

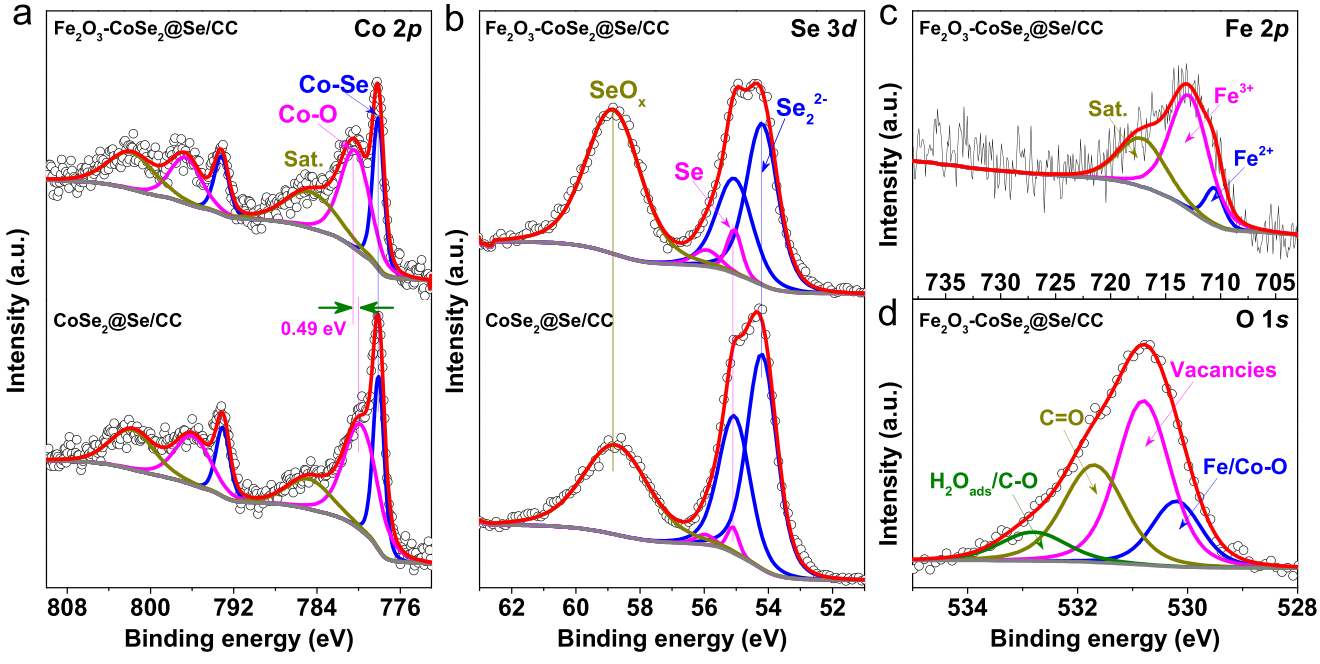

Fig. 3. High-resolution XPS spectra of (a) Co 2*p*, (b) Se 3*d* and (c) Fe 2*p* from Fe_2O_3-$CoSe_2$@Se/CC and $CoSe_2$@Se/CC.

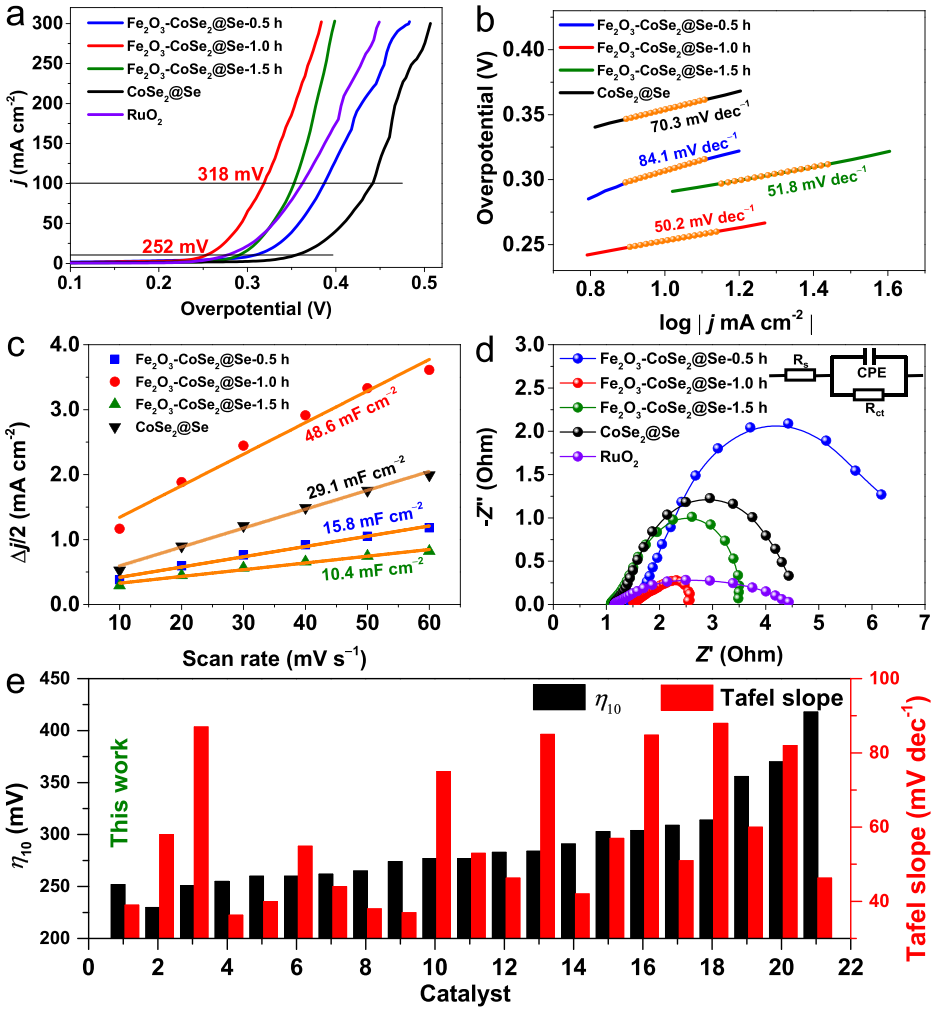

Fig. 4. OER performance of different catalysts conducted in 1.0 M KOH. (a) LSV polarization curves with a scan rate of 5 mV s^{-1}. (b) Corresponding OER Tafel plots. (c) Double-layer capacitance of different catalysts with various scan rates from 10 to 60 mV s^{-1}. (d) Corresponding electrochemical impedance spectroscopy (EIS). The inset is an electrical equivalent circuit used to simulate the impedance data. (e) Compared with the previously reported catalysts overpotentials (η_{10}) at 10 mA cm^{-2} and Tafel slopes (Table S4).

[53], where the specific capacitance of flat surfaces (C_s) is usually found in the range of 20–60 μF cm^{-2}_{geo} [24]. As expected, the Fe_2O_3-$CoSe_2$@Se/CC-1.0 h catalyst retains the maximum ECSA of 1215 cm^2 (normalized to per cm^2 of electrode area), which is much higher than those of Fe_2O_3-$CoSe_2$@Se-0.5 h (395 cm^2), Fe_2O_3-$CoSe_2$@Se-1.5 h (260 cm^2), and $CoSe_2$@Se (720 cm^2). The values of C_{dl} and ECSA are close to those of some recently reported Co-based electrocatalysts (**Table S3**). In addition, as shown in Fig. 4**d,** the inset R_s represents solution resistance and R_{ct} represents charge transfer impedance. The R_{ct} of Fe_2O_3-$CoSe_2$@Se/CC-1.0 h catalyst has the smallest charge transfer resistance among all the other catalysts (**Table S5**), indicating that the hybrid catalyst has the highest conductivity, which intrinsically contributes to the enhancement of OER catalytic performance [54]. More broadly, the OER performance of Fe_2O_3-$CoSe_2$@Se/CC-1.0 h is also comparable to most of reported Co-based OER catalysts in terms of η_{10} and Tafel slope (Fig. 4**e**), **Table S4** [55–57].

The change of TOF values along with overpotential for different catalysts are discussed in Fig. 5**a**. As the overpotential increases, the TOF values of all catalysts increase monotonically. Moreover, at OER overpotentials of 300 mV and 350 mV, the TOF values of Fe_2O_3-$CoSe_2$@Se/CC-1.0 h catalyst are much higher than all control catalysts (Fig. 5**b**), once again confirming the highest intrinsic catalytic oxygen evolution conversion efficiency [24]. The O_2 gas is collected quantitatively by drainage and compared with the theoretical value calculated according to Faraday's law (Fig. 5**c**) [58,59]. As shown in Fig. 5**d**, the measured O_2 content maintains a steady increasing trend. For Fe_2O_3-$CoSe_2$@Se/CC-1.0 h, the Faradaic efficiency (FE) of O_2 is similar to the theoretical value.

The industrial application potential is investigated by an electrochemical system with two-electrode configuration using Fe_2O_3-$CoSe_2$@Se/CC as the anode and Pt/C as the cathode to construct a cell for overall water splitting. In Fig. 6**a**, the Fe_2O_3-$CoSe_2$@Se/$CC^{(+)}$||Pt/$C^{(-)}$ electrolyzer delivers a current density of 10 and 100 mA cm^{-2} at a cell voltage of 1.58 and 1.69 V in 1.0 M KOH solution, superior to most of the previously reported two-electrode catalytic systems, especially at high current density (Fig. 6**b**), **Table S6**.

To evaluate the stability of the catalyst, the chronopotentiometric curves of Fe_2O_3-$CoSe_2$@Se/CC catalyst were studied in detail. The long-term stability is initially measured at constant current density of 10 mA cm^{-2} (Fig. 6**c**). It was found that the catalyst retained approximately 84.3% of its initial stability after 70 h of continuous operation at a current density of 10 mA cm^{-2}. The before and after OER samples' SEM, TEM, and XPS characterizations show significant alterations in surface morphology (**Fig. S6**) and elemental chemical states (**Fig. S7**). However, there is no significant decline in the OER performance, suggesting the catalyst reaches a particular equilibrium

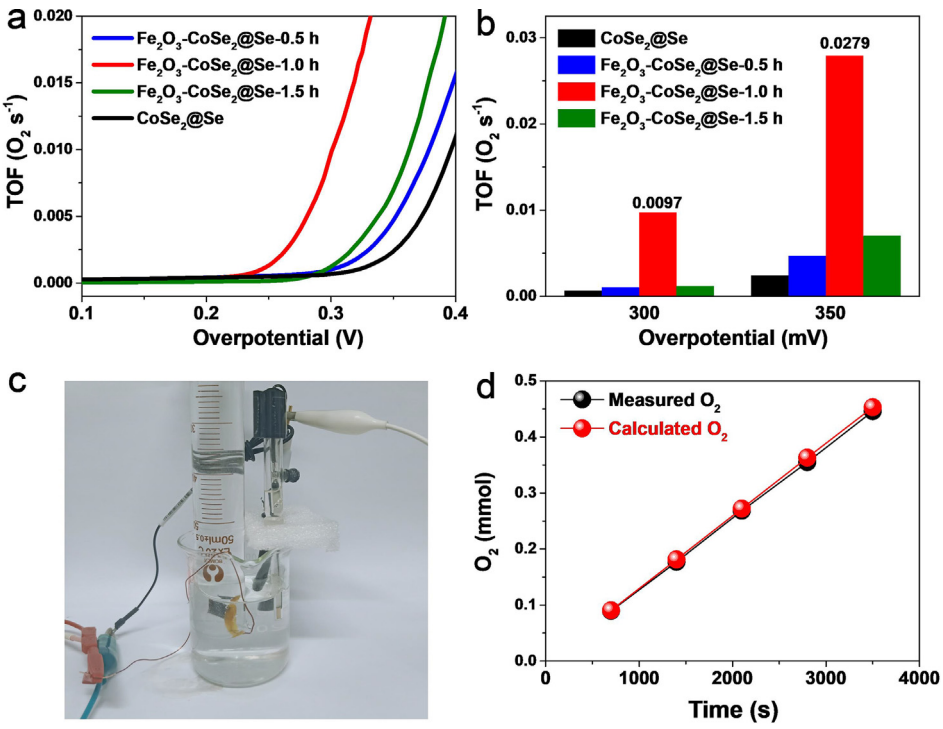

Fig. 5. (a) The turnover frequency (TOF) profiles versus overpotential of various catalysts. (b) The TOF values at different overpotentials. (c) The O_2 collection device by drainage, and (b) the amount of O_2 theoretically calculated and experimentally measured versus time.

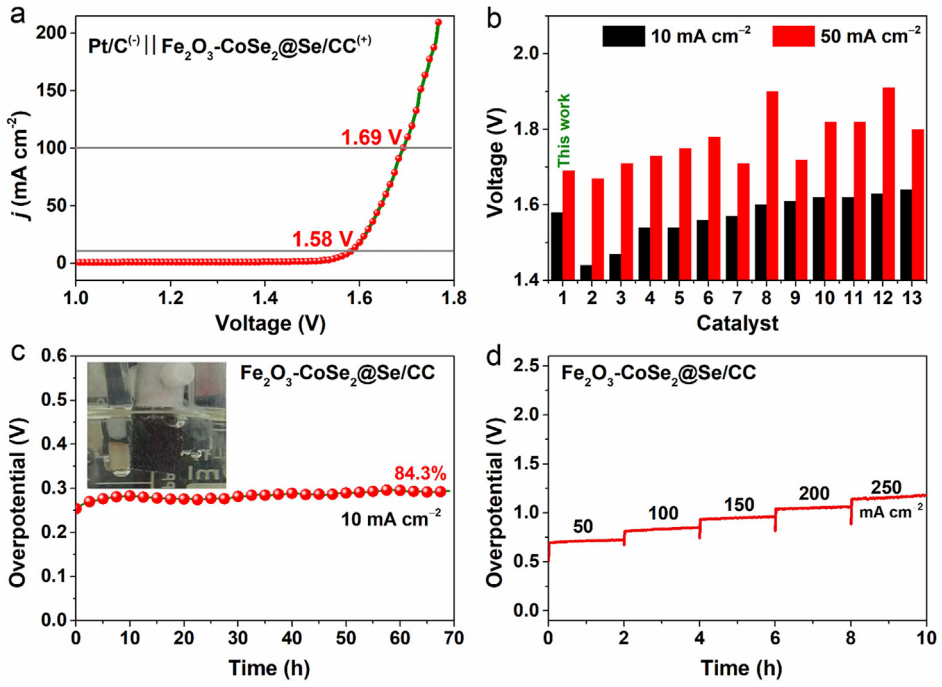

Fig. 6. (a) Overall water splitting of Fe_2O_3-$CoSe_2$@Se/CC (anode) and commercial Pt/C (cathode) in two-electrode system. (b) Comparison with previously reported two-electrode catalysts at 10 and 50 mA cm^{-2} (Table S6). (c) Stability test at 10 mA cm^{-2} for 70 h in three-electrode system. (d) The multi-step chronopotentiometric curves with the change of current densities from 50 to 250 mA cm^{-2} in 1.0 M KOH.

state during OER that is different from the initial state. On changing the current density from 50 to 350 mA cm^{-2} in steps of 50 mA cm^{-2} every 2 h (Fig. 6**d**), we observed small increases in overpotential at the different current densities. These results indicate that the Fe_2O_3-$CoSe_2$@Se/CC electrocatalyst has excellent durability, which may be attributed to the unique coral-like structure and good electrical conductivity [60]. The above results further highlighted that the 3D coral-like Fe_2O_3-$CoSe_2$@Se/CC catalyst possesses excellent OER activity.

Based on the above analysis, a four-electron pathway is suggested for overall OER reaction: $4OH^-$ (aq) → O_2 (g) + $2H_2O$ (aq) + $4e^-$ [45]. Overall, the following features of the electrocatalyst are expected to contribute to its superior performance: (i) The three-dimensional coral-like structure, with a high observed ECSA, helps to expose more active sites as well as improve electrolyte transport and gas emission. (ii) The designed hybrid structure has a smaller electron transfer resistance and provides higher conductivity. This is also reflected in the observed low overpotential. (iii) The $Fe_2O_3/CoSe_2$ heterostructure offers more accessible active sites, thereby synergistically promoting the OER performance [61]. (iv) The observed strong electronic interactions among the different components of the catalyst system along with the high content of oxygen vacancies can modulate the binding energies between the reaction intermediates and the active sites in the OER process, thereby improving the electrocatalytic performance [62].

4. Conclusion

In summary, we successfully prepared a novel catalyst of Fe_2O_3-$CoSe_2$@Se/CC through a conventional hydrothermal growth and soaking treatment. In the case of the optimized hybrid catalyst, XRD confirmed its crystal structure, SEM showed a three-dimensional coral-like structure, and XPS demonstrated strong electronic interactions between different components. The electrocatalytic OER study showed that the hybrid catalyst has excellent electrocatalytic activity and stability in an alkaline three-electrode system, which is also observed in the simulated industrial two-electrode overall water splitting. The study revealed that the hybrid material, with its unique structure, is a promising candidate for industrial electrolysis of water for hydrogen production. Furthermore, this work also provides a feasible route for developing other novel and efficient catalysts.

CRediT authorship contribution statement

Zixia Wan: Investigation, Methodology. **Qiuting He:** Investigation, Data curation. **Yuan Qu:** Data curation. **Jiaxin Dong:** Investigation, Data curation. **Elvis Shoko:** Writing – review & editing. **Puxuan Yan:** Methodology. **Tayirjan Taylor Isimjan:** Writing – review & editing. **Xiulin Yang:** Supervision, Writing – review & editing.

Declaration of Competing Interest

The authors declare that they have no known competing financial interests or personal relationships that could have appeared to influence the work reported in this paper.

Acknowledgements

This work has been supported by the National Natural Science Foundation of China (no. 21965005), Natural Science Foundation of Guangxi Province (2018GXNSFAA294077, 2021GXNSFAA076001), Project of High-Level Talents of Guangxi (F-KA18015), and Guangxi Technology Base and Talent Subject (GUIKE AD18126001, GUIKE AD20297039). Innovation and entrepreneurship training for college students (202110602011).

Appendix A. Supplementary data

Supplementary data to this article can be found online at https://doi.org/10.1016/j.jelechem.2021.115928.

References

[1] R. Gao, D. Yan, Recent Development of Ni/Fe-Based Micro/Nanostructures toward Photo/Electrochemical Water Oxidation, Adv. Energy Mater. 10 (2020) 1900954.
[2] Z. Chen, B. Fei, M. Hou, X. Yan, M. Chen, H. Qing, R. Wu, Ultrathin Prussian blue analogue nanosheet arrays with open bimetal centers for efficient overall water splitting, Nano Energy 68 (2020) 104371.
[3] L. Wang, X. Duan, X. Liu, J. Gu, R. Si, Y. Qiu, Y. Qiu, D. Shi, F. Chen, X. Sun, J. Lin, J. Sun, Atomically Dispersed Mo Supported on Metallic Co_9S_8 Nanoflakes as an Advanced Noble-Metal-Free Bifunctional Water Splitting Catalyst Working in Universal pH Conditions, Adv. Energy Mater. 10 (2020) 1903137.
[4] X.P. Wang, H.J. Wu, S.B. Xi, W.S.V. Lee, J. Zhang, Z.H. Wu, J.O. Wang, T.D. Hu, L. M. Liu, Y. Han, S.W. Chee, S.C. Ning, U. Mirsaidov, Z.B. Wang, Y.W. Zhang, A. Borgna, J. Wang, Y.H. Du, Z.G. Yu, S.J. Pennycook, J.M. Xue, Strain stabilized nickel hydroxide nanoribbons for efficient water splitting, Energy Environ. Sci. 13 (2020) 229–237.
[5] C. Defilippi, D.V. Shinde, Z. Dang, L. Manna, C. Hardacre, A.J. Greer, C. D'Agostino, C. Giordano, HfN Nanoparticles: An Unexplored Catalyst for the Electrocatalytic Oxygen Evolution Reaction, Angew. Chem. Int. Ed. 58 (2019) 15464–15470.
[6] X. Wang, H. Zhang, Z. Yang, C. Zhang, S. Liu, Ultrasound-treated metal-organic framework with efficient electrocatalytic oxygen evolution activity, Ultrason. Sonochem. 59 (2019) 104714.
[7] J.M.V. Nsanzimana, L. Gong, R. Dangol, V. Reddu, V. Jose, B.Y. Xia, Q. Yan, J.-M. Lee, X. Wang, Tailoring of Metal Boride Morphology via Anion for Efficient Water Oxidation, Adv. Energy Mater. 9 (2019) 1901503.
[8] M.-T. Chen, J.-J. Duan, J.-J. Feng, L.-P. Mei, Y. Jiao, L. Zhang, A.-J. Wang, Iron, rhodium-codoped Ni_2P nanosheets arrays supported on nickel foam as an efficient bifunctional electrocatalyst for overall water splitting, J. Colloid Interface Sci. 605 (2022) 888–896.
[9] J.-J. Duan, Z. Han, R.-L. Zhang, J.-J. Feng, L. Zhang, Q.-L. Zhang, A.-J. Wang, Iron, manganese co-doped Ni_3S_2 nanoflowers in situ assembled by ultrathin nanosheets as a robust electrocatalyst for oxygen evolution reaction, J. Colloid Interface Sci. 588 (2021) 248–256.
[10] R.-L. Zhang, J.-J. Duan, J.-J. Feng, L.-P. Mei, Q.-L. Zhang, A.-J. Wang, Walnut kernel-like iron-cobalt-nickel sulfide nanosheets directly grown on nickel foam: A binder-free electrocatalyst for high-efficiency oxygen evolution reaction, J. Colloid Interface Sci. 587 (2021) 141–149.
[11] Y. Liu, C. Ma, Q. Zhang, W. Wang, P. Pan, L. Gu, D. Xu, J. Bao, Z. Dai, 2D Electron Gas and Oxygen Vacancy Induced High Oxygen Evolution Performances for Advanced Co_3O_4/CeO_2 Nanohybrids, Adv. Mater. 31 (2019) 1900062.
[12] G. Shen, R. Zhang, L. Pan, F. Hou, Y. Zhao, Z. Shen, W. Mi, C. Shi, Q. Wang, X. Zhang, J.-J. Zou, Regulating Spin State of Fe(III) by Atomically Anchoring on Ultrathin Titanium Dioxide for Efficient Oxygen Evolution Electrocatalysis, Angew. Chem. Int. Ed. 59 (2020) 2313–2317.
[13] T. Tian, H. Gao, X. Zhou, L. Zheng, J. Wu, K. Li, Y. Ding, Study of the Active Sites in Porous Nickel Oxide Nanosheets by Manganese Modulation for Enhanced Oxygen Evolution Catalysis, ACS Energy Lett. 3 (2018) 2150–2158.
[14] Y. Yang, L. Dang, M.J. Shearer, H. Sheng, W. Li, J. Chen, P. Xiao, Y. Zhang, R.J. Hamers, S. Jin, Highly Active Trimetallic NiFeCr Layered Double Hydroxide Electrocatalysts for Oxygen Evolution Reaction, Adv. Energy Mater. 8 (2018) 1703189.
[15] Y. Shi, Y. Yu, Y. Liang, Y. Du, B. Zhang, In Situ Electrochemical Conversion of an Ultrathin Tannin Nickel Iron Complex Film as an Efficient Oxygen Evolution Reaction Electrocatalyst, Angew. Chem. Int. Ed. 58 (2019) 3769–3773.
[16] A. El Arrassi, Z. Liu, M.V. Evers, N. Blanc, G. Bendt, S. Saddeler, D. Tetzlaff, D. Pohl, C. Damm, S. Schulz, K. Tschulik, Intrinsic Activity of Oxygen Evolution Catalysts Probed at Single $CoFe_2O_4$ Nanoparticles, J. Am. Chem. Soc. 141 (2019) 9197–9201.
[17] C. Liang, P. Zou, A. Nairan, Y. Zhang, J. Liu, K. Liu, S. Hu, F. Kang, H.J. Fan, C. Yang, Exceptional Performance of Hierarchical Ni-Fe Oxyhydroxide@NiFe Alloy Nanowire Array Electrocatalyst for Large Current Density Water Splitting, Energy Environ. Sci. 13 (2020) 86–95.
[18] N. Yu, W. Cao, M. Huttula, Y. Kayser, P. Hoenicke, B. Beckhoff, F. Lai, R. Dong, H. Sun, B. Geng, Fabrication of FeNi hydroxides double-shell nanotube arrays with enhanced performance for oxygen evolution reaction, Appl. Catal. B: Environ. 261 (2020) 118193.
[19] J. Saha, S. Verma, R. Ball, C. Subramaniam, R. Murugavel, Compositional Control as the Key for Achieving Highly Efficient OER Electrocatalysis with Cobalt Phosphates Decorated Nanocarbon Florets, Small 16 (2020) 1903334.
[20] X. Zou, Y. Liu, G.D. Li, Y. Wu, D.P. Liu, W. Li, H.W. Li, D. Wang, Y. Zhang, X. Zou, Ultrafast Formation of Amorphous Bimetallic Hydroxide Films on 3D Conductive Sulfide Nanoarrays for Large-Current-Density Oxygen Evolution Electrocatalysis, Adv. Mater. 29 (2017) 1700404.
[21] S. Esmailzadeh, T. Shahrabi, G. Barati Darband, Y. Yaghoubinezhad, Pulse electrodeposition of nickel selenide nanostructure as a binder-free and high-efficient catalyst for both electrocatalytic hydrogen and oxygen evolution reactions in alkaline solution, Electrochim. Acta 334 (2020) 135549.
[22] A.T. Swesi, J. Masud, M. Nath, Nickel selenide as a high-efficiency catalyst for oxygen evolution reaction, Energy Environ. Sci. 9 (2016) 1771–1782.
[23] Y. Hu, H. Yu, L. Qi, J. Dong, P. Yan, T. Taylor Isimjan, X. Yang, Interface Engineering of Needle-Like P-Doped MoS_2/CoP Arrays as Highly Active and Durable Bifunctional Electrocatalyst for Overall Water Splitting, ChemSusChem 14 (2021) 1565–1573.
[24] B. Wang, H. Huang, M. Huang, P. Yan, T.T. Isimjan, X. Yang, Electron-transfer enhanced MoO_2-Ni heterostructures as a highly efficient pH-universal catalyst for hydrogen evolution, Sci. China Chem. 63 (2020) 841–849.
[25] P. Yan, M. Huang, B. Wang, Z. Wan, M. Qian, H. Yan, T.T. Isimjan, J. Tian, X. Yang, Oxygen defect-rich double-layer hierarchical porous Co_3O_4 arrays as high-efficient

oxygen evolution catalyst for overall water splitting, J. Energy Chem. 47 (2020) 299–306.
[26] B. Wang, H. Huang, T. Sun, P. Yan, T.T. Isimjan, J. Tian, X. Yang, Dissolution reconstruction of electron-transfer enhanced hierarchical NiS_x-MoO_2 nanosponges as a promising industrialized hydrogen evolution catalyst beyond Pt/C, J. Colloid Interface Sci. 567 (2020) 339–346.
[27] Z. Wan, H. Yu, Q. He, Y. Hu, P. Yan, X. Shao, T.T. Isimjan, B. Zhang, X. Yang, In-situ growth and electronic structure modulation of urchin-like Ni–Fe oxyhydroxide on nickel foam as robust bifunctional catalysts for overall water splitting, Int. J. Hydrogen Energy 45 (2020) 22427–22436.
[28] P. Ge, H. Hou, S. Li, L. Huang, X. Ji, Three-Dimensional Hierarchical Framework Assembled by Cobblestone-Like $CoSe_2$@C Nanospheres for Ultrastable Sodium-Ion Storage, ACS Appl. Mater. Interfaces 10 (2018) 14716–14726.
[29] J. Mu, D. Luo, H. Miao, J. Fan, X. Hu, Synergistic wide spectrum response and directional carrier transportation characteristics of $Se/SnSe_2/TiO_2$ multiple heterojunction for efficient photoelectrochemical simultaneous degradation of Cr (VI) and RhB, Appl. Surf. Sci. 542 (2021) 148673.
[30] J. Zhao, Q. Yang, R. Shi, G.I.N. Waterhouse, X. Zhang, L.-Z. Wu, C.-H. Tung, T. Zhang, $FeO–CeO_2$ nanocomposites: an efficient and highly selective catalyst system for photothermal CO_2 reduction to CO, NPG Asia Mater. 12 (2020) 5.
[31] C. Miao, X. Xiao, Y. Gong, K. Zhu, K. Cheng, K. Ye, J. Yan, D. Cao, G. Wang, P. Xu, Facile Synthesis of Metal-Organic Framework-Derived $CoSe_2$ Nanoparticles Embedded in the N-Doped Carbon Nanosheet Array and Application for Supercapacitors, ACS Appl. Mater. Interfaces 12 (2020) 9365–9375.
[32] S. Wang, Y. Zhu, X. Sun, H. Liu, J. Cui, Y. Zhang, W. He, N, S co-doped modified graphene/Fe_2O_3 composites synthesized via microwave-assisted method for Na-ion batteries, Inorg. Chem. Commun. 121 (2020) 108188.
[33] M.A. Ruiz Fresneda, J. Delgado Martín, J. Gómez Bolívar, M.V. Fernández Cantos, G. Bosch-Estévez, M.F. Martínez Moreno, M.L. Merroun, Green synthesis and biotransformation of amorphous Se nanospheres to trigonal 1D Se nanostructures: impact on Se mobility within the concept of radioactive waste disposal, Environ. Sci.: Nano 5 (2018) 2103–2116.
[34] X. Peng, F. Gao, J. Zhao, J. Li, J. Qu, H. Fan, Self-assembly of a graphene oxide/$MnFe_2O_4$ motor by coupling shear force with capillarity for removal of toxic heavy metals, J. Mater. Chem. A 6 (2018) 20861–20868.
[35] S. Fan, G. Li, F. Cai, G. Yang, Synthesis of Porous Ni-Doped $CoSe_2$/C Nanospheres towards High-Rate and Long-Term Sodium-Ion Half/Full Batteries, Chem. Eur. J. 26 (2020) 8579–8587.
[36] Y. Pan, X. Cheng, M. Gao, Y. Fu, J. Feng, L. Gong, H. Ahmed, H. Zhang, V.S. Battaglia, Cagelike $CoSe_2$@N-Doped Carbon Aerogels with Pseudocapacitive Properties as Advanced Materials for Sodium-Ion Batteries with Excellent Rate Performance and Cyclic Stability, ACS Appl. Mater. Interfaces 12 (2020) 33621–33630.
[37] Q. Gan, B. Wang, J. Chen, J. Tian, T.T. Isimjan, X. Yang, Exploring the effect of Ni/Cr contents on the sheet-like NiCr-oxide-decorated CNT composites as highly active and stable catalysts for urea electrooxidation, Clean Energy 4 (2020) 58–66.
[38] Y.-P. Chen, S.-Y. Lin, R.-M. Sun, A.-J. Wang, L. Zhang, X. Ma, J.-J. Feng, FeCo/FeCoP encapsulated in N, Mn-codoped three-dimensional fluffy porous carbon nanostructures as highly efficient bifunctional electrocatalyst with multi-components synergistic catalysis for ultra-stable rechargeable Zn-air batteries, J. Colloid Interface Sci. 605 (2022) 451–462.
[39] Y. Dou, C.-T. He, L. Zhang, H. Yin, M. Al-Mamun, J. Ma, H. Zhao, Approaching the activity limit of $CoSe_2$ for oxygen evolution via Fe doping and Co vacancy, Nat. Commun. 11 (2020) 1664.
[40] S.H. Yang, S.-K. Park, Y.C. Kang, MOF-Derived $CoSe_2$@N-Doped Carbon Matrix Confined in Hollow Mesoporous Carbon Nanospheres as High-Performance Anodes for Potassium-Ion Batteries, Nano-Micro Lett. 13 (2020) 9.
[41] J. Guo, B. Wang, D. Yang, Z. Wan, P. Yan, J. Tian, T.T. Isimjan, X. Yang, Rugae-like Ni_2P-CoP nanoarrays as a bi-functional catalyst for hydrogen generation: $NaBH_4$ hydrolysis and water reduction, Appl. Catal. B: Environ. 265 (2020) 118584.
[42] H. Li, D. Gao, X. Cheng, Simple microwave preparation of high activity Se-rich $CoSe_2$/C for oxygen reduction reaction, Electrochim. Acta 138 (2014) 232–239.
[43] J.K. Kim, G.D. Park, J.H. Kim, S.K. Park, Y.C. Kang, Rational Design and Synthesis of Extremely Efficient Macroporous $CoSe_2$-CNT Composite Microspheres for Hydrogen Evolution Reaction, Small 13 (2017) 1700068.
[44] Z. Wan, Q. He, J. Chen, T.T. Isimjan, B. Wang, X. Yang, Dissolution-regrowth of hierarchical Fe-Dy oxide modulates the electronic structure of nickel-organic frameworks as high-active and stable water splitting electrocatalysts, Chinese, J. Catal. 41 (2020) 1745–1753.
[45] Z. Wan, D. Yang, J. Chen, J. Tian, T.T. Isimjan, X. Yang, Oxygen-Evolution Catalysts Based on Iron-Mediated Nickel Metal-Organic Frameworks, ACS Appl. Nano Mater. 2 (2019) 6334–6342.
[46] S. Gao, F. Liao, S. Ma, L. Zhu, M. Shao, Network-like mesoporous $NiCo_2O_4$ grown on carbon cloth for high-performance pseudocapacitors, J. Mater. Chem. A 3 (2015) 16520–16527.
[47] K. Zhu, F. Shi, X. Zhu, W. Yang, The roles of oxygen vacancies in electrocatalytic oxygen evolution reaction, Nano Energy 73 (2020) 104761.
[48] Y. Zhang, F. Ye, W.-D.-Z. Li, Self-Assembled Two-Dimensional NiO/CeO_2 Heterostructure Rich in Oxygen Vacancies as Efficient Bifunctional Electrocatalyst for Alkaline Hydrogen Evolution and Oxygen Evolution, Chem. Eur. J. 27 (2021) 3766–3771.
[49] G. Zhao, K. Rui, S.X. Dou, W. Sun, Boosting electrochemical water oxidation: the merits of heterostructured electrocatalysts, J. Mater. Chem. A 8 (2020) 6393–6405.
[50] X. Zheng, X. Han, Y. Cao, Y. Zhang, D. Nordlund, J. Wang, S. Chou, H. Liu, L. Li, C. Zhong, Y. Deng, W. Hu, Identifying Dense $NiSe_2/CoSe_2$ Heterointerfaces Coupled with Surface High-Valence Bimetallic Sites for Synergistically Enhanced Oxygen Electrocatalysis, Adv. Mater. 32 (2020) 2000607.
[51] K. Zhang, S. Deng, Y. Zhong, Y. Wang, J. Wu, X. Wang, X. Xia, J. Tu, Rational construction of cross-linked porous nickel arrays for efficient oxygen evolution reaction, Chin. J. Catal. 40 (2019) 1063–1069.
[52] X. Li, W. Xue, R. Mo, S. Yang, H. Li, J. Zhong, In situ growth of minimal Ir-incorporated $Co_xNi_{1-x}O$ nanowire arrays on Ni foam with improved electrocatalytic activity for overall water splitting, Chin. J. Catal. 40 (2019) 1576–1584.
[53] S.L. Zhang, B.Y. Guan, X.F. Lu, S. Xi, Y. Du, X.W.D. Lou, Metal Atom-Doped Co_3O_4 Hierarchical Nanoplates for Electrocatalytic Oxygen Evolution, Adv. Mater. 32 (2020) 2002235.
[54] L. Wu, L. Yu, X. Xiao, F. Zhang, S. Song, S. Chen, Z. Ren, Recent Advances in Self-Supported Layered Double Hydroxides for Oxygen Evolution Reaction, Research 2020 (2020) 3976278.
[55] Z. Xia, H. Sun, X. He, Z. Sun, C. Lu, J. Li, Y. Peng, S. Dou, J. Sun, Z. Liu, In situ construction of CoSe2@vertical-oriented graphene arrays as self-supporting electrodes for sodium-ion capacitors and electrocatalytic oxygen evolution, Nano Energy 60 (2019) 385–393.
[56] Y. Zhu, H.-C. Chen, C.-S. Hsu, T.-S. Lin, C.-J. Chang, S.-C. Chang, L.-D. Tsai, H.M. Chen, Operando Unraveling of the Structural and Chemical Stability of P-Substituted $CoSe_2$ Electrocatalysts toward Hydrogen and Oxygen Evolution Reactions in Alkaline Electrolyte, ACS Energy Lett. 4 (2019) 987–994.
[57] Z. Zou, T. Wang, X. Zhao, W.-J. Jiang, H. Pan, D. Gao, C. Xu, Expediting in-Situ Electrochemical Activation of Two-Dimensional Metal-Organic Frameworks for Enhanced OER Intrinsic Activity by Iron Incorporation, ACS Catal. 9 (2019) 7356–7364.
[58] B. Lu, J. Zang, W. Li, J. Li, Q. Zou, Y. Zhou, Y. Wang, Co-doped Ni_xP_y loading on Co_3O_4 embedded in Ni foam as a hierarchically porous self-supported electrode for overall water splitting, Chem. Eng. J. 422 (2021) 130062.
[59] Z. Liu, D. Liu, L. Zhao, J. Tian, J. Yang, L. Feng, Efficient overall water splitting catalyzed by robust $FeNi_3N$ nanoparticles with hollow interiors, J. Mater. Chem. A 9 (2021) 7750–7758.
[60] M. Yu, Z. Wang, J. Liu, F. Sun, P. Yang, J. Qiu, A hierarchically porous and hydrophilic 3D nickel–iron/MXene electrode for accelerating oxygen and hydrogen evolution at high current densities, Nano Energy 63 (2019) 103880.
[61] X. Li, Y. Wang, J. Wang, Y. Da, J. Zhang, L. Li, C. Zhong, Y. Deng, X. Han, W. Hu, Sequential Electrodeposition of Bifunctional Catalytically Active Structures in MoO_3/Ni–NiO Composite Electrocatalysts for Selective Hydrogen and Oxygen Evolution, Adv. Mater. 32 (2020) 2003414.
[62] M.-I. Jamesh, M. Harb, Tuning the electronic structure of the earth-abundant electrocatalysts for oxygen evolution reaction (OER) to achieve efficient alkaline water splitting – A review, J. Energy Chem. 56 (2021) 299–342.